AIP | Review of Scientific Instruments

A hyperspectral imaging system for an accurate prediction of the above-ground biomass of individual rice plants

Hui Feng, Ni Jiang, Chenglong Huang, Wei Fang, Wanneng Yang et al.

Citation: Rev. Sci. Instrum. **84**, 095107 (2013); doi: 10.1063/1.4818918
View online: http://dx.doi.org/10.1063/1.4818918
View Table of Contents: http://rsi.aip.org/resource/1/RSINAK/v84/i9
Published by the AIP Publishing LLC.

A hyperspectral imaging system for an accurate prediction of the above-ground biomass of individual rice plants

Hui Feng,[1] Ni Jiang,[1] Chenglong Huang,[1] Wei Fang,[1] Wanneng Yang,[2,3] Guoxing Chen,[4] Lizhong Xiong,[2] and Qian Liu[1,a)]

[1]*Britton Chance Center for Biomedical Photonics, Wuhan National Laboratory for Optoelectronics-Huazhong University of Science and Technology, 1037 Luoyu Rd., Wuhan 430074, People's Republic of China*
[2]*National Key Laboratory of Crop Genetic Improvement and National Center of Plant Gene Research, Huazhong Agricultural University, Wuhan 430070, People's Republic of China*
[3]*College of Engineering, Huazhong Agricultural University, Wuhan 430070, People's Republic of China*
[4]*MOA Key Laboratory of Crop Ecophysiology and Farming System in the Middle Reaches of the Yangtze River, College of Plant Science and Technology, Huazhong Agricultural University, Wuhan, Hubei 430070, China*

(Received 19 June 2013; accepted 5 August 2013; published online 11 September 2013)

Biomass is an important component of the plant phenomics, and the existing methods for biomass estimation for individual plants are either destructive or lack accuracy. In this study, a hyperspectral imaging system was developed for the accurate prediction of the above-ground biomass of individual rice plants in the visible and near-infrared spectral region. First, the structure of the system and the influence of various parameters on the camera acquisition speed were established. Then the system was used to image 152 rice plants, which selected from the rice mini-core collection, in two stages, the tillering to elongation (T-E) stage and the booting to heading (B-H) stage. Several variables were extracted from the images. Following, linear stepwise regression analysis and 5-fold cross-validation were used to select effective variables for model construction and test the stability of the model, respectively. For the T-E stage, the R^2 value was 0.940 for the fresh weight (FW) and 0.935 for the dry weight (DW). For the B-H stage, the R^2 value was 0.891 for the FW and 0.783 for the DW. Moreover, estimations of the biomass using visible light images were also calculated. These comparisons showed that hyperspectral imaging performed better than the visible light imaging. Therefore, this study provides not only a stable hyperspectral imaging platform but also an accurate and nondestructive method for the prediction of biomass for individual rice plants. © *2013 AIP Publishing LLC*. [http://dx.doi.org/10.1063/1.4818918]

I. INTRODUCTION

Rice is the staple food for much of the world's population.[1,2] Considering the growing needs of the world population, increasing crop yields is one of the main goals of research into the rice plant. Biomass is an important component of the plant phenomics and is important for the calculation of the basis growth rate and production.[3] The above-ground fresh weight (FW) and dry weight (DW) are methods for accurately measuring biomass in the studies of individual plants.

Traditional methods of measuring the FW and DW are destructive, time-consuming, and labor-intensive, so they are not suitable for large-scale phenotyping experiments. Moreover, it is impossible to take a series of measurement on the same plant at different points during its life cycle.[4] So researchers came up with several nondestructive methods for measuring biomass, such as visible light imaging and spectral imaging. Golzarian *et al.*[4] proposed a biomass estimation method for barley and wheat using the sum of the projected areas of three orthogonal views and the plant age. However, this method did not distinguish between the different organs of the plant. Conversely, the spectral reflectance of visible and near-infrared wavelengths is closely related to the produce indices that are sensitive to biochemical and biophysical variations in vegetation.[5,6] The vegetation index is a popular indicator for predicting biomass in the field of remote sensing,[7–10] but it is primarily used to predict biomass over large areas in the field of remote sensing and cannot fully exploit the rich information of hyperspectral data. In general, spectral methods use multispectral imaging[10] or point sampling with a spectroradiometer.[7]

Hyperspectral imaging is an emerging and nondestructive technology that can acquire spectral and spatial information simultaneously. Compared with visible light imaging and multispectral imaging, hyperspectral imaging has a high spectral resolution and has become a powerful tool in many fields of agricultural research.[11] Hyperspectral imaging systems (HIS) have been used in the characterization of vegetation spectral features,[12] dry matter yield predictions,[13] the inspection of poultry carcasses,[14] the early detection of spoilage in mandarins,[15] and the prediction of moisture content in dehydrated prawns.[16] To the best of our knowledge, there is no hyperspectral imaging system capable of predicting the biomass of individual rice plants. To measure the biomass of individual rice plants nondestructively and more accurately, we have developed a HIS to predict the above-ground biomass of individual rice plants.

a)Author to whom correspondence should be addressed. Electronic mail: qianliu@mail.hust.edu.cn. Tel.: +86 27 87792033. Fax: +86 27 87792034.

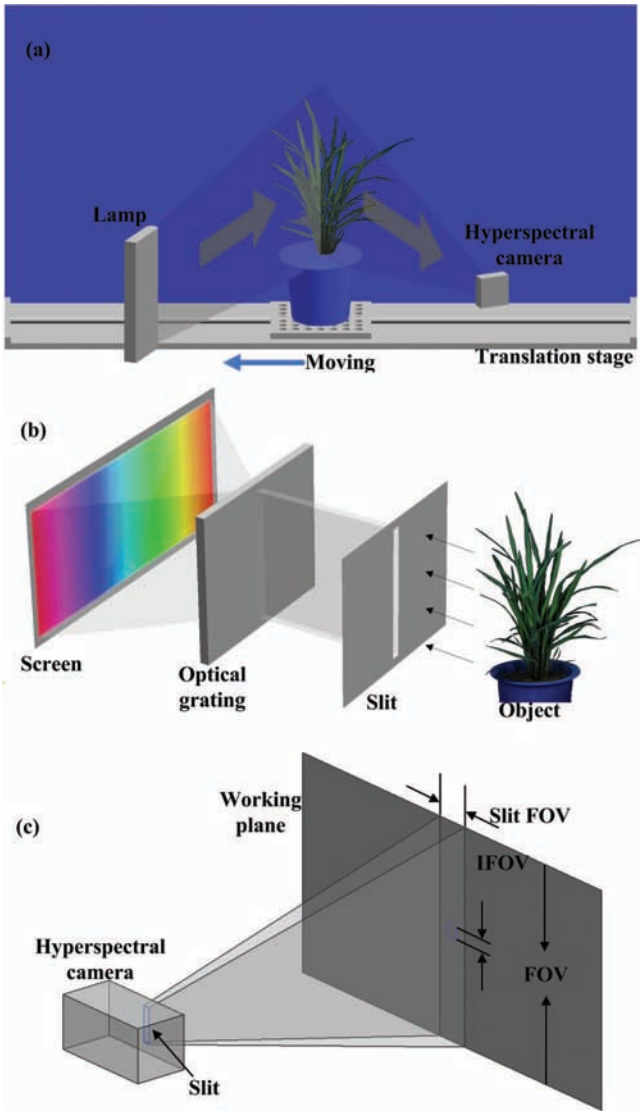

FIG. 1. Diagram of the HIS (a), the internal optical path (b), and the hyperspectral camera field of view (c).

II. SYSTEM DESCRIPTION

A. Hardware design

The HIS developed for this study consisted of a hyperspectral camera, a halogen lamp, a translation stage, and a computer (Fig. 1(a)). The hyperspectral camera consisted of an imaging spectrograph (Hyperspec^{TM} VNIR, Headwall Photonics, USA), an EMCCD sensor (Luca-R, Andor Technology, UK), and an objective lens (23 mm, Schneider Optics, Hauppauge, USA). The spectral range was 400–1000 nm and the spectral resolution was 3.2 nm. The slit width was 25 μm. The line-scan orientation was perpendicular to the slit (Fig. 1(a)). The incoming light was dispersed by the optical grating, so the resulting images included both spectral and spatial information (Fig. 1(b)). The size of the EMCCD was 1004 × 1002 pixels, and the pixel size was 8 × 8 (μm^2). The halogen lamp (380–1700 nm, Headwall Hyperspec Starter Kit-VNIR, USA) was a line source next to the camera. The maximum stroke of the translation stage (BHMS02-50A, Bohongzhida, China) was 500 mm. The speed was adjustable according to the size of the object distance and the camera acquisition speed, which is discussed in Sec. II B. A computer equipped with 2.96 GB RAM and an Intel Core CPU (2.8 GHz) was used for system control and data analysis. To increase the accuracy of background separation from the plant, a blue backdrop was used, and the system was operated in a darkroom.

To ensure a full scan of a potted rice plant for the tillering to elongation (T-E) stage and the booting to heading (B-H) stage, the field of view (FOV) needed to be 1.0 m (Fig. 1(c)). So the working distance was set to 2.9 m (calculated using Eq. (1)). The instantaneous field of view (IFOV, defined by Eq. (2)), which was equivalent to the width of one pixel corresponding to the working plane, was 1.0 mm. Thus, if the acquired image needed to be undeformed for later analysis, the translation stage could be moved to the next 1.0 mm position when the camera finished one line scan. The slit-width field of view (slit FOV, defined by Eq. (3)) was 3.1 mm

$$\text{Working distance} = \frac{f \times H}{h}, \tag{1}$$

$$IFOV = \frac{H}{N_h}, \tag{2}$$

$$\text{Slit } FOV = \frac{\text{slit width}}{\text{pixel size width}} \times IFOV, \tag{3}$$

where f represents the focal length of the camera, H represents the plant height, h represents the height of the EMCCD, and N_h represents the number of EMCCD pixels in the height orientation.

B. Software design

1. System control

The software possessed three major parts: a preparation unit, an acquisition unit, and a saving unit (Fig. 2). The Labview 8.6 (National Instruments, USA) was used to control the system. The operating procedure included the following steps. (1) The camera was initialized. (2) The temperature was set, and the cooler was opened. (3) The current dark data were saved and denoted as I_b. (4) The whiteboard data were saved and denoted as I_w. (5) The kinetics number and the kinetics time were set. (6) The memory was cleared before acquisition. (7) The acquisition was started (Fig. 3), and the translation stage was moved uniformly. The header file was generated at this time. The header file contained the acquisition time, slit width, data length, acquisition frames, wavelength distribution, and data type, so other software, such as Environment for Visualizing Images (Exelis Visual Information Solutions, USA), could read the data. (8) Subsequently, the acquisition data were stored in a binary data stream. If the acquisition did end, then the translation stage would go back to zero. If the raw data acquired by the camera were recorded as I_0, the data saved in the binary file were I (as defined by Eq. (4)). The data of the binary file were thus spectral reflectance. (9) After saving data from one plant, acquisition would start at step (6) if a new plant were to be measured. Otherwise, the program

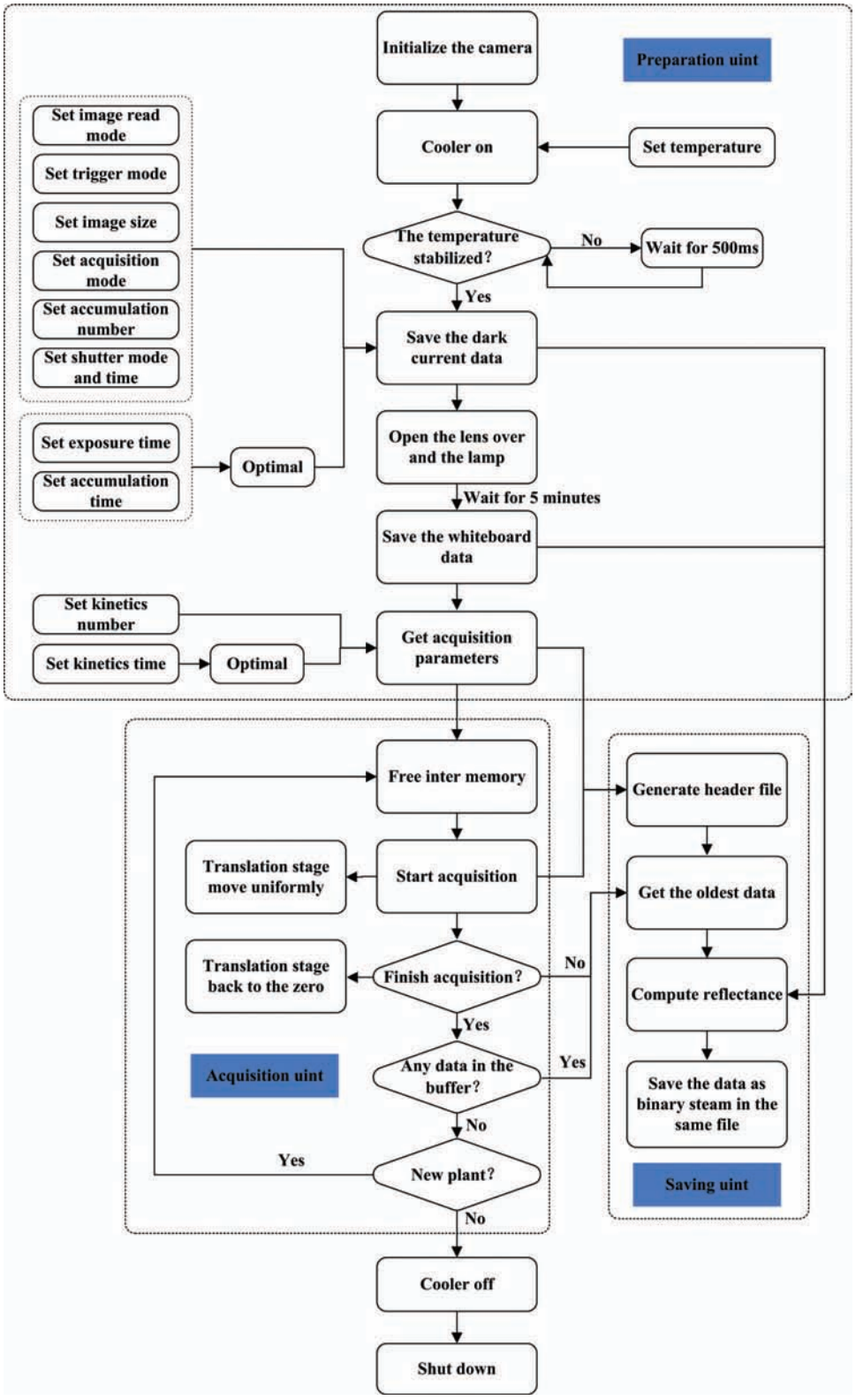

FIG. 2. Diagram of control and data acquisition for the HIS.

would stop

$$I = \frac{I_0 - I_b}{I_w - I_b}, \tag{4}$$

where I_0 indicates the raw data, I_b indicates the dark current data, and I_w indicates the whiteboard data.

2. Settings for main parameters

For the system control and data acquisition depicted in Fig. 2, the parameters image read mode, trigger mode, image size, exposure time, acquisition mode, accumulation time, kinetics number, kinetics time, shutter time, and shutter mode

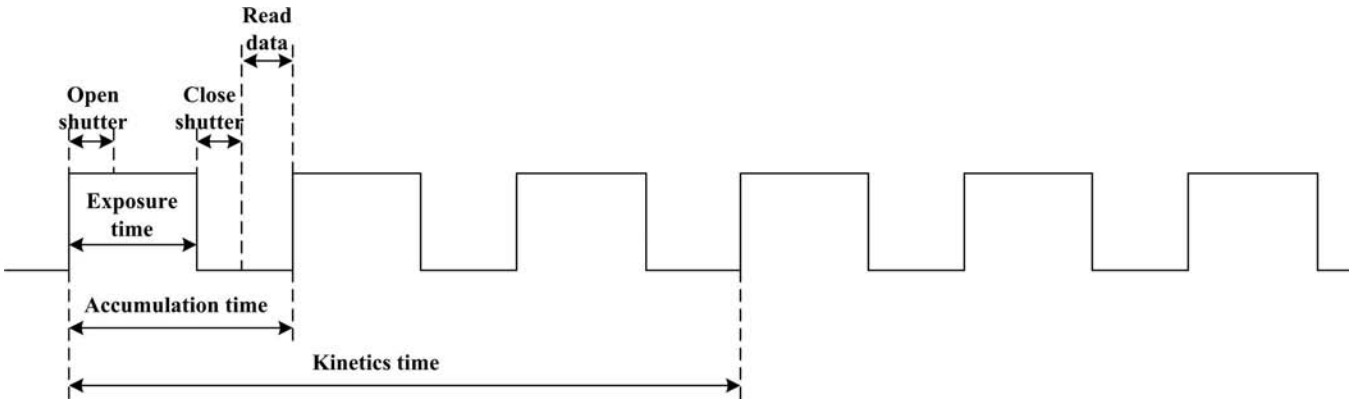

FIG. 3. Timing diagram for camera acquisition.

were set. Of these, image size, exposure time, accumulation number, and kinetic number affected the camera acquisition speed. The image size included hbin and vbin. Hbin controlled the image height, and vbin controlled the number of wavelengths (Eqs. (5) and (6)). Higher values of hbin and vbin resulted in better signal-to-noise ratios. These settings would lower the spatial and spectral resolution, however. Because the slit-width FOV was 3.1 mm and the IFOV was 1 mm, the minimum value of vbin was 3. The accumulation number represented the number of repetitions of each frame (Fig. 3), which implied that the signal-to-noise ratio performance improved as the values increased, while the acquisition speed became slower. The camera acquisition time was equivalent to the kinetics time plus the kinetics number, and the kinetics time was equal to the accumulation time plus the accumulation number. The settings of the main parameters are shown in Table I

$$\text{Plant image size} = [round(1004/hbin)] \times (\text{kinetics number}), \tag{5}$$

$$\text{Wavelength number} = round\ (750/vbin), \tag{6}$$

where *round* represents rounding to the nearest integer, and 750 represents the actual available pixel rows in the EMCCD.

TABLE I. The settings of the main parameters.

Parameters	Value
Temperature	−19 °C
Image read mode	Image
Trigger mode	Internal
Hbin	1
Vbin	4
Exposure time	50 ms
Acquisition mode	Kinetics
Accumulation number	3
Accumulation time	100 ms
Kinetics number	According to the plant width
Kinetics time	300 ms
Shutter mode	Auto shutter
Shutter time	30 ms

3. Image processing and variables extraction

The binary file was a data stream, as shown in Fig. 4, and its internal format contained the first wavelength of the first line, followed by the second wavelength of the first line, interleaved up to the 188th wavelength of the first line. Subsequent lines for each wavelength were stored in a similar fashion. In this data stream, the data had to be re-allocated to reconstruct images. In agreement with the characteristics of the hyperspectral image data, the data from this stream could be extracted to form a three-dimensional matrix (λ, h, w), where λ represented the number of wavelengths (corresponding to Eq. (6)), h represented the height of the image (corresponding to the round (1004/vbin) of Eq. (5)), and w was the kinetics number (Table I), representing the number of frames.

After 188 images were extracted, the following process was to extract the variables from the images. The main steps of this process were as follows (Fig. 5). (1) In the data of the orientation of 0°, a wavelength with the largest difference between the background and foreground was chosen (721 nm in this study), and the OTSU algorithm was then used to extract the plant region of interest (ROI) from the image of this wavelength. (2) The ROI was applied to all 188 images of the different wavelengths. (3) We then calculated the area (S), the total reflectance of the plant ROI ($T_1 - T_{188}$, defined by Eq. (7)), the average reflectance of the plant ROI ($A_1 - A_{188}$, defined by Eq. (8)), the first derivative of the total reflectance of the plant ROI ($dT_1 - dT_{188}$), the second derivative of the total reflectance of the plant ROI ($ddT_1 - ddT_{188}$), the first derivative of the average reflectance of the plant ROI ($dA_1 - dA_{188}$), and the second derivative of the average reflectance of the plant ROI ($ddA_1 - ddA_{188}$) for the 188 images obtained from step (2). (4) Steps (1), (2), and (3) were repeated with the data of the orientation of 90°. (5) Finally, every variable extracted from the rice plant was to take the average of the corresponding variable at the orientation of 0° and 90°. Therefore, each rice plant had 1129 variables

$$T_n = \sum_{(i,j)\in ROI} R_{(n,i,j)}, \tag{7}$$

$$A_n = \frac{T_n}{S}, \tag{8}$$

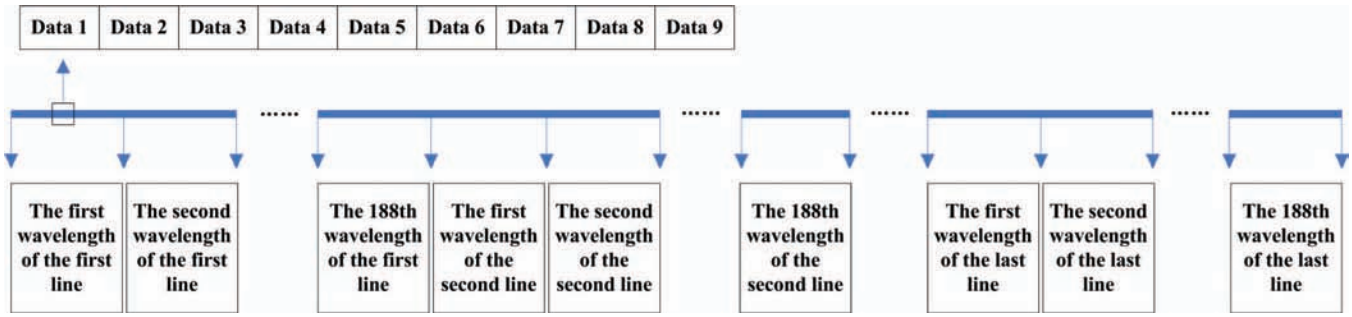

FIG. 4. The format of the binary data stream.

where n indicates the serial number of the 188 images, T_n indicates the total reflectance of the plant ROI for the nth image, A_n indicates the average reflectance of the plant ROI for the nth image, and $R(n, i, j)$ indicates the reflectance of the point with the coordinate (i, j) for the nth image.

III. ABOVE-GROUND BIOMASS PREDICTION OF POTTED RICE

A. Sample preparation

The rice samples were randomly selected from the rice mini-core collection. We chose 152 cultivars, with one pot for

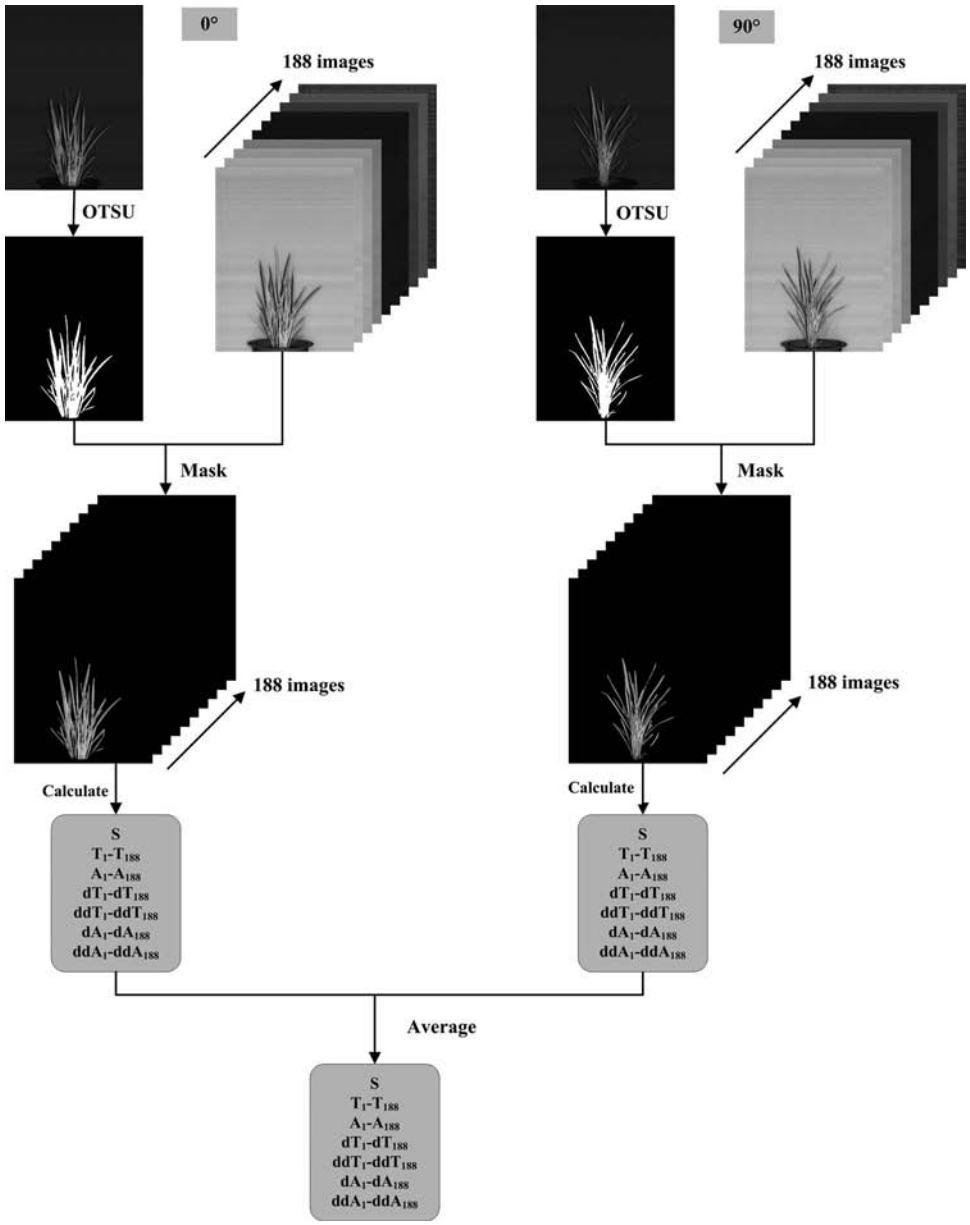

FIG. 5. A diagram of image segmentation and variable extraction.

each cultivar; 76 pots for the T-E stage and 76 pots for the B-H stage.

At each harvest time, 76 randomly selected pots were imaged. Then, the potted rice was harvest to measure the FW and DW with an electronic balance. For the T-E stage, the FW varied between 5.45 g and 85.27 g, and the DW varied between 1.01 g and 17.74 g. For the B-H stage, the FW varied between 52.41 g and 249.92 g, and the DW varied between 8.33 g and 52.17 g. This high diversity in the FW and DW was due to the diversity of cultivars and ensured the validity of the experimental results.

B. Selection of effective independent variables for prediction

After 1129 variables were obtained, linear stepwise regression analysis was used to choose a limited number of variables that mapped with the biomass. Previous studies have demonstrated that fewer effective wavelengths can be equal to or better than a full spread of wavelengths because they contain information relevant to the prediction.[17]

Linear stepwise regression analysis was used when many independent variables had little effect on the dependent variables and some were not completely independent of each other. The purpose of this process was to select effective independent variables for the model and to establish an optimal regression model. Considering the number of samples and the stability of the model, the top four variables were taken as effective independent variables, and other variables were ignored.

C. Model verification

The cross-validation technique was used to measure the estimation error of a predictive model and to assess the prediction error.[18] Cross-validation has been a very robust method. The cross-validation error decreased if only the additional independent variables improved the model prediction for one dataset. The 5-fold cross-validation was used in this study and repeated 10 times to avoid randomicity for grouping. The final step was to average the data from the 10 repeats. Finally, the average R^2 of the modeling set, the mean absolute percentage error (MAPE, defined by Eq. (9)), and the root-mean-square error (RSME, defined by Eq. (10)) of the prediction set were obtained

$$MAPE = \frac{1}{n} \times \sum_{i=1}^{n} \left| \frac{Y_i - y_i}{Y_i} \right| \times 100\%, \tag{9}$$

$$RMSE = \sqrt{\frac{\sum_{i=1}^{n} (Y_i - y_i)^2}{n-1}}, \tag{10}$$

where Y_i indicates the actual value, y_i indicates the prediction value, and n indicates the numbers of samples.

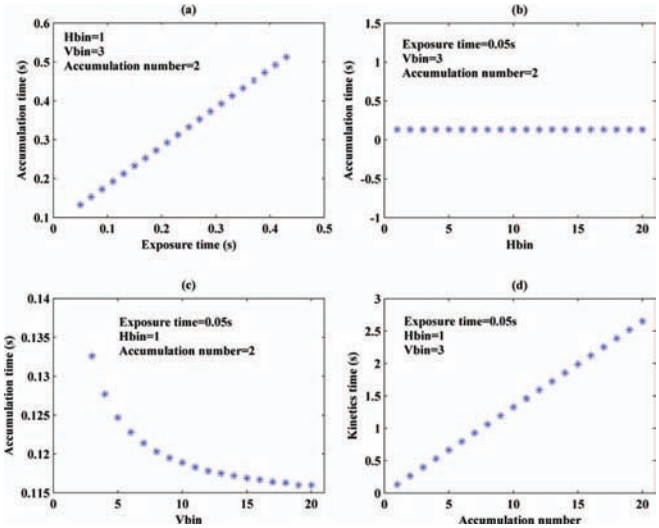

FIG. 6. (a)–(d) The performance of different parameters impacted the acquisition speed.

IV. RESULTS AND DISCUSSION

A. Camera acquisition speed performance

Fig. 6 shows the impact of the *exposure time*, *hbin*, *vbin*, and *accumulation number* on the camera acquisition speed. As observed from Fig. 6, the *exposure time* had the most obvious impact on the acquisition speed. *Hbin* had no effect on the acquisition speed, and *vbin* had a limited impact on the acquisition speed compared with the exposure time. The shorter *exposure times* permitted faster acquisition speeds. However, if the *exposure time* was set to be too short, then the quality of the acquired image deteriorated. Considering the acquisition speed and image quality, the appropriate parameters were set to collect data (Table I).

B. Spectral features of potted rice plants

Fig. 7 shows the spectral reflectance from the hyperspectral images of the whole rice plant. The actual original spectral range of the system was 400–1000 nm, but the camera was more sensitive to the near-infrared region. Additionally, the region between 400 and 470 nm had a relatively high noise level. Therefore, the data from 400 to 470 nm were removed. The trends for the total reflectance (Figs. 7(a) and 7(g)) and the average reflectance (Figs. 7(b) and 7(h)) curves of the different cultivars were similar in the same period, except the differences among the total reflectance of different varieties were more obvious than differences among the average reflectance of different varieties. For the same stage, the relationship among the total reflectance curves of different varieties differed from the relationship among the average reflectance curves of different varieties. This result may indicate that the differences among the different varieties could not be explained by just the area. The total reflectance of the B-H stage was larger than the T-E stage, perhaps because there were more new leaves growing on the plant.

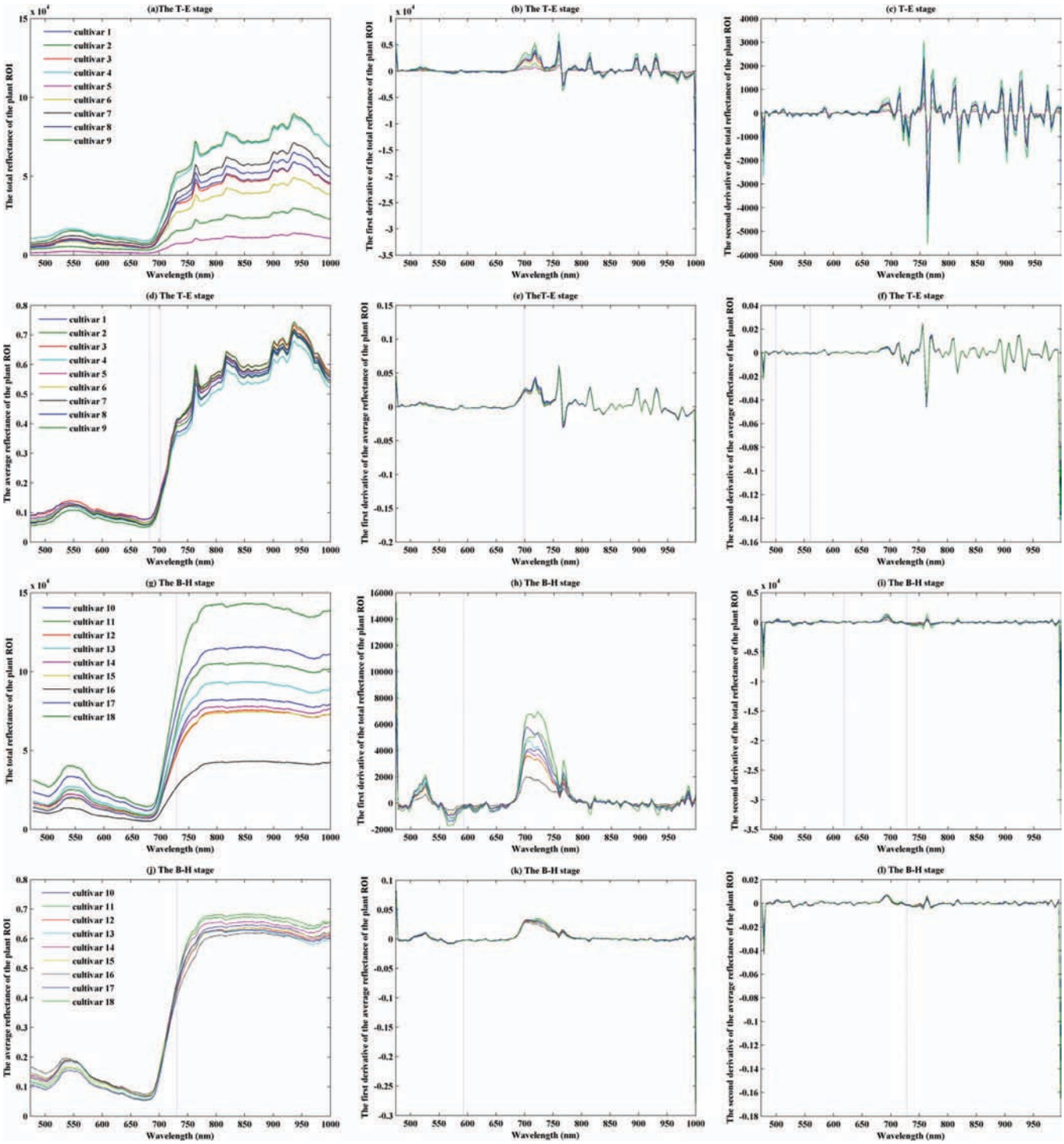

FIG. 7. (a)–(l) Spectral reflectance from the hyperspectral images of the whole rice plant. The dashed lines represent the effective independent variables.

C. Effective independent variables selection and modeling

Effective independent variables were selected based on linear stepwise regression analysis. For the T-E stage, the variables selected for the FW were S, A_{96} (705 nm, Fig. 7(d)), ddA_{63} (560 nm, Fig. 7(f)), and A_{89} (683 nm, Fig. 7(d)), and the variables selected for the DW were S, dA_{94} (699 nm, Fig. 7(e)), dT_{38} (519 nm, Fig. 7(b)), and ddA_{32} (500 nm, Fig. 7(f)). For the B-H stage, the variables selected for the FW were S, ddT_{102} (725 nm, Fig. 7(i)), A_{104} (731 nm, Fig. 7(j)), and ddT_{69} (619 nm, Fig. 7(i)), and the variables selected for the DW were T_{103} (728 nm, Fig. 7(g)), dT_{61} (593 nm, Fig. 7(h)), dA_{61} (593 nm, Fig. 7(k)), and ddA_{102} (725 nm, Fig. 7(l)). Notably, the variable S was not in the model for the DW of the B-H stage. Thus, the hyperspectral data were important in the prediction of biomass. Because the spectral resolution was 3.2 nm, the spectral reflectance of adjacent wavelengths had a high correlation coefficient. Therefore, the wavelengths of the selected variables could all be

TABLE II. Performances of 5-fold cross-validation using four independent variables for the T-E and the B-H stages.

Stage	Dependent variable	Independent variable	Prediction set MAPE (%)	Prediction set RMSE (g)	Modeling set average R^2
The T-E stage	FW	S, A_{96}, ddA_{63}, A_{89}	7.85	4.17	0.940
	DW	S, dA_{94}, dT_{38}, ddA_{32}	8.98	0.87	0.935
The B-H stage	FW	S, ddT_{102}, A_{104}, ddT_{69}	8.41	14.51	0.891
	DW	T_{103}, dT_{61}, dA_{61}, ddA_{102}	12.91	4.38	0.783

attributed to several wavelengths: 500 nm, 519 nm, 560 nm, 593 nm, 619 nm, 683 nm, 702 nm, and 728 nm (Fig. 7). These wavelengths were mainly in the visible region, except for 728 nm, which was in the red edge position. These results illustrated that the reflectance of these wavelengths had a relationship with plant biomass. First, the reflectance of different parts of the rice plant was not the same. The chlorophyll content of the stem was lower than the leaves, so the reflectance of the stem at 400–1000 nm was higher than that of the leaves. Second, the leaf reflectance was not the same either. Some of the leaves overlapped, leading to additional reflectance relative to other parts of the plant. Moreover, as can be observed in Fig. 7, the selected variables were mostly the first and second derivatives of the reflectance at the inflection point of the derivative curves. Normally, the derivative represents the rate of change. Thus, the selected independent variables were the mutation of the reflectance. Horler *et al.*[19] found that the first derivative of the reflectance of wavelength 725 nm had a linear relationship with the leaf mass using spectrophotometry. Previous studies have found that a wavelength of approximately 550 nm was a reflection valley for green plants. In our research, the wavelengths 560 nm and 728 nm were very close to the above results. The other wavelength that our research identified may be an important wavelength for determining the biomass of individual rice plants. These results suggest that the reflectance observed at these wavelengths was the most effective at detecting the biomass of the individual rice plants.

After selecting four effective independent variables, an analysis of variance was used to test the difference between the independent variables and dependent variable. The result showed that the models were reliable.

D. Modeling validation

To evaluate the performance of our model for biomass prediction, 5-fold cross-validation was used. The validation results are shown in Table II, and the scatter plot is shown in Fig. 8. For the T-E stage, the MAPE and RMSE were 7.85% and 4.17 g for the FW, respectively, and 8.98% and 0.87 g for the DW, respectively. For the B-H stage, the MAPE and RMSE were 8.41% and 14.51 g for the FW, respectively, and 12.91% and 4.38 g for the DW, respectively. The average R^2 value for the FW and DW modeling sets were 0.940 and 0.935 for the T-E stage, respectively, and 0.891 and 0.783 for the B-H stage, respectively. These calculations demonstrate that these four variables predict the biomass levels well. When only using the variable *S* to predict the T-E stage biomass, the average R^2 value for the modeling set was 0.851 for the FW and 0.884 for the DW. For the B-H stage, the average R^2 value for the modeling set was 0.807 for the FW and 0.609 for the DW (data not shown). Clearly, the model containing added spectral variables produced a better result. Therefore, additional spectral variables could significantly improve the accuracy of biomass prediction.

E. Comparisons with other methods

The method that was used to predict above-ground biomass in the field of remote sensing has been discussed previously. Boelman *et al.*[20] used the Normalized Difference Vegetation Index (NDVI) and the above-ground biomass (defined by Eq. (11)) to perform a linear regression and found that the linear regression coefficient between the NDVI and the above-ground biomass was $r^2 = 0.84$. The NDVI was thus used in this study to calculate the linear regression coefficient with the above-ground biomass. As observed in Table III, the regression coefficient was very small. Therefore, the NDVI was not suitable for the prediction of above-ground biomass for individual rice plants

$$NDVI = (R_{800} - R_{660})/(R_{800} + R_{660}), \quad (11)$$

where R_{800} represents the reflectance at 800 nm (a near-infrared wavelength), and R_{660} represents the reflectance at 660 nm (a visible red wavelength).

The method used for the analysis of hyperspectral data was principal component analysis (PCA). Therefore, we used PCA to analyze the raw data. Then, the principal components were used to perform linear stepwise regression analysis. Finally, 5-fold cross-validation was used to test the accuracy of the model. These results are shown in Table IV. The results from Table IV are significantly worse than the results presented in Table II. Therefore, the variable with most of information may not have been the most effective. Moreover, the results from Table IV confirmed the results of Sec. III C; the selected variable had neither the largest nor the smallest extreme data points.

In addition, we also estimated the biomass of the same plants using the APPF method (Golzarian *et al.*[4]) and compared the performance of the method with that of ours.

TABLE III. The regression coefficient between NDVI and above-ground biomass.

Stage	Dependent variable	Regression coefficient(r^2)
The T-E stage	FW	0.002
	DW	0.02
The B-H stage	FW	0.13
	DW	0.0008

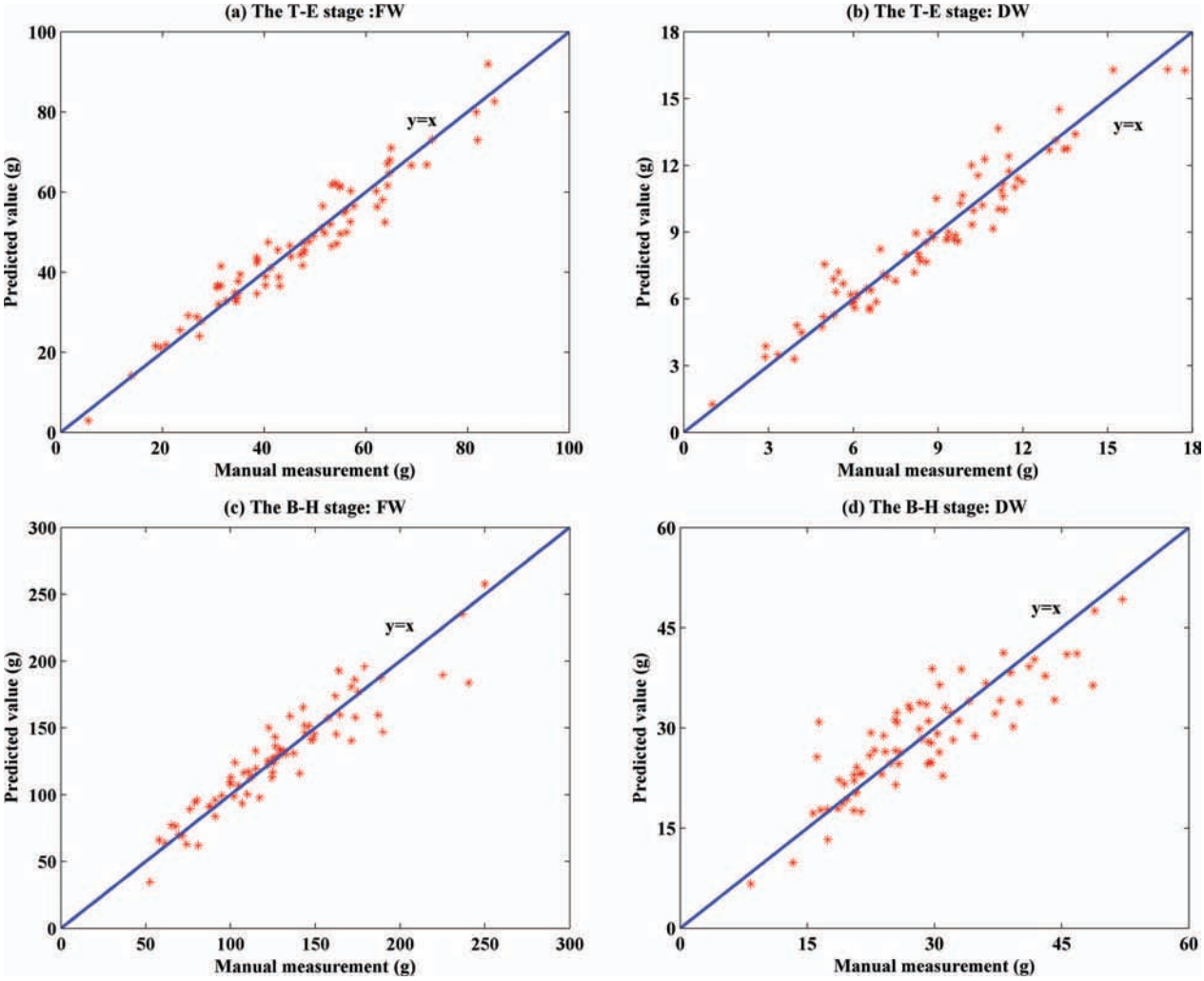

FIG. 8. Performance of 5-fold cross-validation using four variables for the (a) and (b) T-E and (c) and (d) B-H stages.

The method of Australian Plant Phenomics Facility (APPF) is depicted in the following equation:

$$W = a_0 + a_1 \times (S_1 + S_2 + S_{top}) + a_2 \times (S_1 + S_2 + S_{top}) \times T_{day}, \quad (12)$$

where w represents the weight (g), S_1 represents the side projected area of 0°, S_2 represents the side projected area of 90°, S_{top} represents the top projected area, and T_{day} represents the plant age in days after planting. The images were acquired using H-SMART combined with the visible light technique.[21] Table V shows the performance of 5-fold cross-validation using the APPF method. For the T-E stage, the average R^2 values for the modeling set were 0.878 for the FW and 0.876 for the DW. For the B-H stage, the average R^2 values for the modeling set were 0.797 for the FW and 0.656 for the DW. These results were close to the results observed using the variable S. The visible light image had a higher resolution than the hyperspectral image and could add the topside feature, but it could not provide the spectral information. In our work, spectral information with a relationship to biomass, not just area information, was added to the model. Moreover, the total reflectance of the plant ROI may explain that every point of the plant ROI has a weight, so this variable can explain the different organs of the plant. Therefore, we recovered a smaller error and a better result. Overall, the HIS provided better performance for individual rice plants.

TABLE IV. Performance of 5-fold cross-validation with PCA and linear stepwise regression analysis.

Stage	Dependent variable	Independent variable	Prediction set MAPE (%)	Prediction set RMSE (g)	Modeling set average R^2
The T-E stage	FW	PC1, PC5, PC6, PC2	12.30	6.49	0.868
	DW	PC1, PC5, PC2, PC7	11.81	1.21	0.890
The B-H stage	FW	PC3, PC1, PC8, PC2	9.79	16.28	0.879
	DW	PC3, PC1, PC2, PC82	13.60	4.65	0.786

TABLE V. Performances of 5-fold cross-validation using the APPF method.

Stage	Dependent variable	Independent variable	Prediction set MAPE (%)	Prediction set RMSE (g)	Modeling set average R^2
The T-E stage	FW	$S_1 + S_2 + S_{top}$, $(S_1 + S_2 + S_{top}) \times T_{day}$	11.25	6.18	0.878
	DW	$S_1 + S_2 + S_{top}$, $(S_1 + S_2 + S_{top}) \times T_{day}$	12.41	1.25	0.876
The B-H stage	FW	$S_1 + S_2 + S_{top}$, $(S_1 + S_2 + S_{top}) \times T_{day}$	13.66	20.15	0.797
	DW	$S_1 + S_2 + S_{top}$, $(S_1 + S_2 + S_{top}) \times T_{day}$	17.16	5.62	0.656

V. CONCLUSION

This study was performed to develop a HIS for the accurate prediction of rice above-ground biomass in early stages of growth. The structure of the system and the influence of various parameters on the camera acquisition speed were established, and we obtained accurate predictions for the above-ground biomass of rice plants with this system. In addition, the system also has the potential to characterize other phenotypic traits (e.g., green leaf area) or physiological parameters (e.g., chlorophyll) of cereal plants nondestructively. However, these results were produced in a single season. Therefore, these results should be replicated in future studies across several years to ascertain the robustness of this method for the prediction of above-ground biomass for individual rice plants.

ACKNOWLEDGMENTS

This work was supported by grants from the Program for New Century Excellent Talents in University (No. NCET-10-0386), the National Program on High Technology Development (2012AA10A303), National Program for Basic Research of China (2012CB114305), and the National Natural Science Foundation of China (NNSFC) (30921091 and 31200274).

[1]Q. Zhang, Proc. Natl. Acad. Sci. U.S.A. **104**, 16402 (2007).
[2]W. Yang, L. Duan, G. Chen, L. Xiong, and Q. Liu, Curr. Opin. Plant Biol. **16**, 180 (2013).
[3]O. Tackenberg, Ann. Bot. (London) **99**, 777 (2007).
[4]M. R. Golzarian, R. A. Frick, K. Rajendran, B. Berger, S. Roy, M. Tester, and D. S. Lun, Plant Methods. **7**, 2 (2011).
[5]G. Asrar, *Theory and Applications of Optical Remote Sensing* (John Wiley and Sons, New York, 1989), p. 734.
[6]P. S. Thenkabail, R. B. Smith, and E. De Pauw, Remote Sens. Environ. **71**, 158 (2000).
[7]O. Mutanga and A. K. Skidmore, Int. J. Appl. Earth Obs. Geoinfo. **5**, 87 (2004).
[8]M. A. Cho, A. Skidmore, F. Corsi, S. E. Van Wieren, and I. Sobhan, Int. J. Appl. Earth Obs. Geoinfo. **9**, 414 (2007).
[9]G. Maire, C. François, K. Soudani, D. Berveiller, J. Y. Pontailler, N. Bréda, H. Genet, and E. Dufrêne, Remote Sens. Environ. **112**, 3846 (2008).
[10]S. Phinn, C. Roelfsema, A. Dekker, V. Brando, and J. Anstee, Remote Sens. Environ. **112**, 3413 (2008).
[11]J. Li, X. Rao, and Y. Ying, Comput. Electron. Agric. **78**, 38 (2011).
[12]X. Ye, K. Sakai, H. Okamoto, and L. O. Garciano, Comput. Electron. Agric. **63**, 13 (2008).
[13]D. Perbandt, T. Fricke, and M. Wachendorf, Comput. Electron. Agric. **73**, 230 (2010).
[14]S. C. Yoon, B. Park, K. C. Lawrence, W. R. Windham, and G. W. Heitschmidt, Comput. Electron. Agric. **79**, 159 (2011).
[15]J. Gómez-Sanchis, L. Gómez-Chova, N. Aleixos, G. Camps-Valls, C. Montesinos-Herrero, E. Moltó, and J. Blasco, J. Food Eng. **89**, 80 (2008).
[16]D. Wu, H. Shi, S. Wang, Y. He, Y. Bao, and K. Liu, Anal. Chim. Acta **726**, 57 (2012).
[17]X. Zhang and Y. He, Ind. Crops Prod. **42**, 416 (2013).
[18]R. Kohavi, Int. Jt. Conf. Artif. Intell. **14**, 1137 (1995).
[19]D. N. H. Horler, M. Dockray, and J. Barber, Int. J. Remote Sens. **4**, 273 (1983).
[20]N. T. Boelman, M. Stieglitz, H. M. Rueth, M. Sommerkorn, K. L. Griffin, G. R. Shaver, and J. A. Gamon, Oecologia **135**, 414 (2003).
[21]W. Yang, X. Xu, L. Duan, Q. Luo, S. Chen, S. Zeng, and Q. Liu, Rev. Sci. Instrum. **82**, 025102 (2011).